RESEARCH ARTICLE

Key Points:
- A concise matrix operator framework is developed for analysis of numerical water tracer experiments
- Transport is split into local divergence and remote convergence terms, which are further decomposed
- Applying the framework to a global climate model experiment yields new insights on moisture transport

Correspondence to:
H. A. Singh,
hansi@atmos.washington.edu

A mathematical framework for analysis of water tracers: Part 1: Development of theory and application to the preindustrial mean state

H. A. Singh[1], C. M. Bitz[1], J. Nusbaumer[2], and D. C. Noone[2,3]

[1]Department of Atmospheric Sciences, University of Washington, Seattle, Washington, USA, [2]Department of Atmospheric and Oceanic Sciences, University of Colorado, Boulder, Colorado, USA, [3]Department of Earth, Ocean, and Atmospheric Sciences, Oregon State University, Corvallis, Oregon, USA

Abstract A new matrix operator framework is developed to analyze results from climate modeling studies that employ numerical water tracers (WTs), which track the movement of water in the aerial hydrological cycle from evaporation to precipitation. Model WT output is related to the fundamental equation of hydrology, and the moisture flux divergence is subdivided into the divergence of locally evaporated moisture and the convergence of remotely evaporated moisture. The formulation also separates locally and remotely sourced precipitation. The remote contribution (also the remote moisture convergence) may be further subdivided into zonal, meridional, intrabasin, and interbasin parts. This framework is applied to the preindustrial climate as simulated by a global climate model in which water has been tagged in 10° latitude bands in each of the major ocean basins, and in which each major land mass has been tagged separately. New insights from the method reveal fundamental differences between the major ocean basins in locally sourced precipitation, remotely sourced precipitation, and their relative partitioning. Per unit area, the subtropical Atlantic is the largest global moisture source, providing precipitable water to adjacent land areas and to the eastern Pacific tropics while retaining the least for in situ precipitation. Subtropical moisture is least divergent over the Pacific, which is the smallest moisture source (per unit area) for global land areas. Basins also differ in how subtropical moisture is partitioned between tropical, midlatitude, and land regions. Part II will apply this framework to hydrological cycle perturbations due to CO_2 doubling.

1. Introduction

From evaporation to precipitation, a molecule of water typically spends 9 days in the atmosphere [*Hartmann*, 1994]. Numerical water tracers (WTs), also known as water tags, are a powerful tool for understanding this brief period that water molecules spend in the aerial hydrological cycle. Water tagging in an atmospheric general circulation model (AGCM) involves labeling water vapor at its point of evaporation (or sublimation) and following its movement in an Eulerian sense through the atmosphere until it precipitates. WTs track moisture from its source region, through horizontal and vertical transport by the atmospheric circulation, through phase transitions from vapor to cloud liquid or ice, to its (eventual) point of precipitation. Once water precipitates (i.e., after one evaporation to precipitation cycle), the WT tag is renewed.

The earliest studies to incorporate WTs into AGCMs were those of *Koster et al.* [1986] and *Joussaume et al.* [1986]. Both studies demonstrated that moisture of ocean origin is a significant component of terrestrial precipitation. Both of these studies were limited by short model integrations (less than one season), which were necessary to overcome the prohibitive computational cost associated with WTs at that time.

Following *Koster et al.* [1986] and *Joussaume et al.* [1986], several studies implemented numerical WTs in AGCMs to study precipitation recycling ratios (RRs) and remote source regions [*Numaguti*, 1999; *Bosilovich and Schubert*, 2002; *Bosilovich*, 2002]. Other studies used WTs implemented in mesoscale weather models to consider questions relevant to regional precipitation sources and recycling [see *Sodemann et al.*, 2009; *Knoche and Kunstmann*, 2013; *Sodemann and Stohl*, 2013]. WTs have also been used to aid paleoclimate studies, many of which depend on interpreting the isotopic composition of water in ice cores and sediments to infer local temperature, salinity, and circulation (both atmosphere and ocean). The validity of such

Table 1. Synopsis of Studies in the Literature Employing Numerical WTs, Including the Region on Which the Study Focuses, the Model Used (Either an AGCM, a Global Climate Model, GCM, or a Numerical Weather Prediction Model, NWPM), and a One-Line Summary of the Major Findings

Study	Model	Region	Relevant Findings
Koster et al. [1986]	NASA/GISS GCM 8° × 10°	Global	Seasonal variability in remote source regions; Low-latitude land regions rely more on ocean-sourced moisture
Joussaume et al. [1986]	AGCM	Global	Local recycling is important for inland regions in summer.
Numaguti [1999]	CCSR/NIES AGCM T21	Global (Eurasia)	80% of precipitation inland in summer is from land-sourced moisture; In winter, most inland precipitation is from ocean-sourced moisture
Bosilovich and Schubert [2002]	GEOS-3 GCM 2° × 2.5°	Global (N. America and Eurasia)	Over the midwestern U.S., land-sourced moisture is most important; There is a high correlation between total precipitation and RR
Bosilovich [2002]	(Same as previous)	(Same as previous)	Lower tropospheric water is more locally sourced; Upper tropospheric water is more remotely sourced
Sodemann et al. [2009]	CHRM (NWPM) 0.5° × 0.5°	Europe	Relative importance of moisture-source regions for the Elbe flood (2002) changed over the course of the event.
Sodemann and Stohl [2013]	(Same as previous)	W. Europe, N. Atlantic	Moisture transport by atmospheric rivers is linked to evolution of midlatitude cyclones and upper level flow patterns
Knoche and Kunstmann [2013]	MM5 (NWPM)	W. Africa	Only 3% of the precipitation over the Sahel is from local moisture sources
Koster et al. [1992]	NASA/GISS GCM 8° × 10°	Global with focus on Antarctica	Temperature is more important than source region in determining deuterium excess
Delaygue et al. [2000]	(Same as previous)	Global, LGM and present day	Large seasonal change in Antarctic precipitation source regions; Source regions are sensitive to prescribed low-latitude SSTs
Werner et al. [2001]	ECHAM-5 GCM 3.75° × 3.75°	Global LGM and present day	Antarctic moisture source regions vary by sector; Enhanced source seasonality with LGM boundary conditions
Noone and Simmonds [2002]	Melbourne U AGCM 5.625° × 3.25°	Global	Interannual variability in Antarctic precipitation source regions is coincident with the Southern Annular Mode (SAM)

inferences, however, depends on the source region of precipitated water and the temperature of the source region relative to region of condensation, leading to several modeling studies using WTs to study high-latitude moisture source regions [see, e.g., *Koster et al.*, 1992; *Delaygue et al.*, 2000; *Werner et al.*, 2001; *Noone and Simmonds*, 2002]. Table 1 summarizes previous studies that have used WTs.

Despite their limited use in the literature, numerical WTs may be used to study many aspects of the global hydrological cycle, including remote precipitation sources and their variability (see *Gimeno et al.* [2012] for an overview of various methods for assessing the origin of remote moisture). Indeed, over most land and ocean regions, well over half of the total precipitation has a remote origin [see *Eltahir and Bras*, 1996; *Trenberth*, 1999; *Bosilovich*, 2002]. While moisture recycling may be calculated using atmospheric moisture fluxes [*Brubaker et al.*, 1993], differentiating between remote precipitation sources for a given region is not possible. Recently, Lagrangian back trajectory methods have been used to infer precipitation source regions [*Stohl and James*, 2004, 2009; *Sodemann and Stohl*, 2009; *Brown et al.*, 2012]. Lagrangian back trajectory calculations, however, are very sensitive to the temporal resolution of circulation and moisture fields; high-frequency measurements are essential for minimizing errors and ensuring agreement with Eulerian diagnostics [*Stohl and James*, 2004], and integrations must be carried out over a time period greater than 10 days to obtain accurate estimates of precipitation origin [*Sodemann and Stohl*, 2009]. Numerical WTs, on the other hand, readily reveal where moisture originates.

While WTs provide useful information, several difficulties have curtailed their use. First, WTs are limited by the accuracy of the physics and numerics of the atmospheric models in which they are implemented; any faults and biases in evaporation, convection, cloud processes, tracer advection, and circulation will limit how applicable the WT experimental results are to the real climate system. Second, numerical WTs tend to be computationally expensive. When implemented in a GCM, each tagged region requires a suite of passive tracers (representing, for example, water vapor, cloud liquid, and cloud ice that correspond to the tagged evaporative region) that must be tracked through time and recorded for each grid cell and atmospheric level. If global coverage and relatively fine resolution of source regions is required, hundreds of tracers must be used, often making the desired numerical experiment unfeasible from a computational viewpoint. Finally, large WT experiments constitute a big data problem: an experiment with n tagged regions, for example, minimally requires $\mathcal{O}(n^2)$ tracer exchange coefficients between tagged regions, which are cumbersome and unintuitive to visualize. Such problems require systematic, rather than ad hoc analysis methods, but such methods have remained underdeveloped in the literature.

In this study, we confront this final difficulty by developing a concise and intuitive mathematical framework for analyzing the output of modeling experiments that use WTs. Our framework relies on moisture conservation: in a global time-averaged sense, the amount of moisture that evaporates must be equal to the amount that precipitates. Using basic linear algebra and analysis, we develop a matrix formulation in which the precipitation is written as a function of evaporation from each tagged region, and in which local and remote precipitation sources are separated into distinct terms. We apply this analysis method to a preindustrial GCM experiment. In the process, we use several matrix decomposition methods to analyze the local and remote precipitation source terms, and use these decompositions to gain new insights on the aerial hydrological cycle.

The structure of this study is as follows. In section 2, we develop a concise mathematical framework with which to analyze the output of numerical WT experiments, in section 3, we describe our model run, and in section 4, we use our run to demonstrate the utility of our mathematical framework and to develop it further. We offer some points for discussion and concluding remarks in section 5.

2. Mathematical Development

We seek a framework for using model output from water tagging experiments to understand the mean state and variability of atmospheric water transport in the climate system. We begin with the fundamental equation of hydrology from *Peixoto and Oort* [1992], which is

$$\frac{\partial Q}{\partial t} + \nabla \cdot Q = E - P, \tag{1}$$

where Q denotes column-integrated atmospheric moisture, E denotes evaporation, and P denotes precipitation. In words, we can consider this to be a statement of conservation of Q in the atmosphere, given sources (E) and sinks (P).

For time periods greater than a year, variations in the storage of water in the atmosphere are negligible (relative to the other terms) and the equation becomes

$$\overline{\nabla \cdot Q} = \bar{E} - \bar{P}, \tag{2}$$

where the overbars denote annual climatologies. After integrating globally and applying the divergence theorem, equation (2) becomes

$$\iint_{earth} \overline{\nabla \cdot Q} \ dA = \int \overline{Q \cdot \hat{n}} \ ds = \iint_{earth} (\bar{E} - \bar{P}) \ dA = 0 \ . \tag{3}$$

Thus, over a global domain, we obtain the familiar equality

$$\bar{E} = \bar{P}. \tag{4}$$

Now, consider the hydrology equation for the case of a limited domain i, smaller than global:

$$(\nabla \cdot Q)_i = E_i - P_i. \tag{5}$$

For each region, a fraction of E_i will precipitate locally and contribute to P_i, while another fraction will be exported from the region and will precipitate elsewhere. To describe this, we define an export fraction e_i, which is defined as the fraction of E_i that is precipitated elsewhere, also known as the "aerial runoff." The complement of the aerial runoff, the fraction of locally evaporated water that precipitates locally, is $(1 - e_i)$ (also known as the evaporation recycling ratio) [see *van der Ent et al.*, 2010].

Now, we consider the convergence term. Since evaporated moisture is a conservative quantity, its convergence into region i can be written as the sum of the export from all other regions multiplied by the fraction of that export that enters region i, minus the amount of locally evaporated water that is exported:

$$-(\nabla \cdot Q)_i = \left(\sum_{j, j \neq i} e_j f_{ji} E_j \right) - e_i E_i \tag{6}$$

where e_j is the fraction exported from region j, f_{ji} is the fraction of the export from region j that falls in region i, and E_j is the total evaporation from region j. Note that for a given region j, the sum of these fractions must equal unity,

$$\sum_{i,i\neq j} f_{ji} = 1, \tag{7}$$

and that the fraction of evaporated exported from region j that falls in region j is defined to be nil:

$$f_{jj} = 0. \tag{8}$$

As others have noted when considering the moisture recycling ratio [see, for example, *Brubaker et al.*, 1993; *Eltahir and Bras*, 1996; *Trenberth*, 1998, 1999], the export fraction e_i and its corollary local fraction $(1-e_i)$ are both domain-dependent quantities in that they depend on the size, shape, and spatial orientation of the region considered. If the domain i were the entire globe, for example, the e_i would be zero; decreasing the size of the domain results in e_i asymptotically approaching unity. In Appendix A, we demonstrate that the domain scaling of local and remote contributions to the precipitation is logarithmic, in agreement with previous studies of the precipitation recycling ratio [i.e., *Eltahir and Bras*, 1996; *Brubaker et al.*, 2001; *Dirmeyer and Brubaker*, 2007].

We further note that in our preindustrial control experiment, we have specified tagged spatial domains (10° latitude bands within each ocean basin, with major continental regions tagged separately, as described in section 3) to allow us to isolate the transport of moisture meridionally within each basin and zonally between basins. We have chosen these domains in order to resolve the most interesting physics while utilizing finite computational resources. Zonal transport of evaporated water within a given ocean basin is not accounted for with our choice of spatial domains; any evaporation within one of these domains that falls within the same domain is considered to be local despite substantial zonal moisture transport that may have occurred.

Continuing with our mathematical development, substituting equation (6) into equation (5) yields

$$P_i = E_i + \left(\sum_{j,j\neq i} e_j f_{ji} E_j \right) - e_i E_i. \tag{9}$$

Now, suppose that we have n tagged regions. After rearrangement, this yields a set of equations that may be written compactly in matrix form as

$$\vec{P} = \vec{E} - (\mathbf{I} - \mathbf{F})\mathbf{T}\vec{E} , \tag{10}$$

where $\mathbf{T}$ is the export matrix, whose diagonal entries are equal to e_i, the fraction of vapor evaporated in i that diverges, and whose nondiagonal entries are nil; $\mathbf{I}$ is the identity matrix; $\mathbf{F}$ is the convergence matrix, whose diagonal entries are zero and whose (i,j) th entry $(i \neq j)$ is equal to f_{ji}, the fraction of exported atmospheric water from region j that is precipitated in region i; and $\vec{P}$ and $\vec{E}$ are vectors with entries P_i and E_i, respectively.

Equation (10) may also be written as

$$\vec{P} = \vec{E} - \mathbf{T}\vec{E} + \mathbf{F}\mathbf{T}\vec{E} , \tag{11}$$

which gives three different contributions to the precipitation for a given region: the local evaporation ($\vec{E}$), the local evaporation that diverges ($-\mathbf{T}\vec{E}$), and the remote evaporation that converges ($\mathbf{F}\mathbf{T}\vec{E}$).

In this framework, the fraction of the local precipitation that originates locally may be written as

$$RR = \frac{\vec{E} - \mathbf{T}\vec{E}}{\vec{P}} , \tag{12}$$

which agrees with the flux form of the recycling ratio developed in *Brubaker et al.* [1993]. Unlike *Brubaker et al.* [1993], the area dependence of this quantity is implicit in the area of the tagged source region rather than existing as a free parameter. In Appendix A, we show that the recycling ratio for a given tagged region scales logarithmically with region area.

Using equation (11), we may define the matrix operator

$$\mathbf{M} = \mathbf{I} - (\mathbf{I} - \mathbf{F})\mathbf{T} , \tag{13}$$

which we will use in conjunction with the forward methods described in section 4.5 to compute the precipitation $\vec{P}$ given a particular spatial pattern of $\vec{E}$.

We consider the correspondence between the equations we have developed, (10) and (11), and the customary representation of atmospheric water conservation, equation (1). Equation (1) requires that we have some understanding of the dynamic moisture term $\nabla \cdot Q$, which, in turn, depends on knowing the specific humidity and wind velocity at different atmospheric levels and at short time intervals. In contrast, our formalism enables us to write this term as

$$-\nabla \cdot Q = (\mathbf{FT} - \mathbf{T})\vec{E}. \tag{14}$$

In this development, precipitation sourced from remote regions that is transported by atmospheric motions is contained in **T**, the export matrix, and **F**, the convergence matrix. Evaporation, on the other hand, is the sole thermodynamic contribution to the precipitation; evaporation is, in effect, rearranged by atmospheric motions to produce the resulting pattern of precipitation. By synthesizing information about evaporated water from each of our source regions, we bypass all considerations of the specific pathway by which moisture travels through the atmosphere and only consider the endpoints.

3. Model Experiment Setup

We use the fully coupled Community Earth System Model (CESM) version 1.2 [*Hurrell et al.*, 2013] in which the atmosphere component, Community Atmosphere Model version 5.0 (CAM5) [see *Neale et al.*, 2012], has been refined to include water tagging capability. The methodology used to add WTs to the model is as described in J. Nusbaumer and D. Noone (The sources of moisture for atmospheric rivers that impact the west coast of the united states for both the modern era and 2100, manuscript in preparation, 2016), and is similar to that described in *Koster et al.* [1986], *Joussaume et al.* [1986], *Bosilovich and Schubert* [2002], and *Noone and Simmonds* [2002]. Water evaporated (or sublimated) over each tagged region is tracked in all aspects of the models hydrologic cycle, including surface fluxes, condensation processes, and atmospheric transport. The advected tracer quantity used for each tagged water type at each grid point and atmospheric level is the ratio of the mass of the total tagged water type to the mass of the air. For water vapor only, this would be equivalent to the specific humidity of the tagged water type, although cloud liquid and cloud ice is advected as well. Transport by boundary layer turbulence and large-scale advection occurs without loss, and thus the tagged water types are treated as conservative tracers. Being passive tracers, the WTs do not affect the mean state climate or any of the variables therein, and are evolved by the modeled atmospheric dynamics and physics (Nusbaumer and Noone, manuscript in preparation, 2016).

Our simulation is performed with CAM5 at a $0.9° \times 1.25°$ spatial resolution, with the finite-volume dynamical core. Concentrations of greenhouse gases, ozone, volcanic constituents, and solar insolation are held at preindustrial levels, and atmospheric aerosols are evolved in prognostic mode. The coupled Community Land Model version 4.0 includes full carbon-nitrogen cycling. The ocean and sea ice components are on a displaced-pole grid at nominally $1°$ spatial resolution with the north pole singularity centered on Greenland. The ocean component is fully dynamic and is described in full by *Danabasoglu et al.* [2012]. Subgrid-scale ocean eddies are parameterized with the GM90 eddy diffusion scheme [*Gent and McWilliams*, 1992], with the GM coefficient varying in space and time [*Danabasoglu et al.*, 2012]. The sea ice is fully thermodynamic and dynamic [*Hunke and Lipscomb*, 2004].

Tagged regions are shown in Figure 1, tagged ocean regions are specified in Table 2, and tagged land regions are specified in Table 3. In brief, every $10°$ latitude band in each of the major ocean basins (Atlantic, Pacific, and Indian) is given its own tag. For tagging purposes, the Arctic Ocean is subdivided into Atlantic and Pacific regions, and the Southern Ocean is subdivided into Indian, Pacific, and Atlantic regions. There are a total of 39 distinct tagged ocean regions. Each continent is tagged separately, with North America and Eurasia each subdivided at $45°$N for two tags each.

The tagged run was branched from year 1200 of a preindustrial control simulation, and was integrated for 45 years. The last 30 years were used to construct the annually averaged and seasonal climatologies that we use in the following analysis.
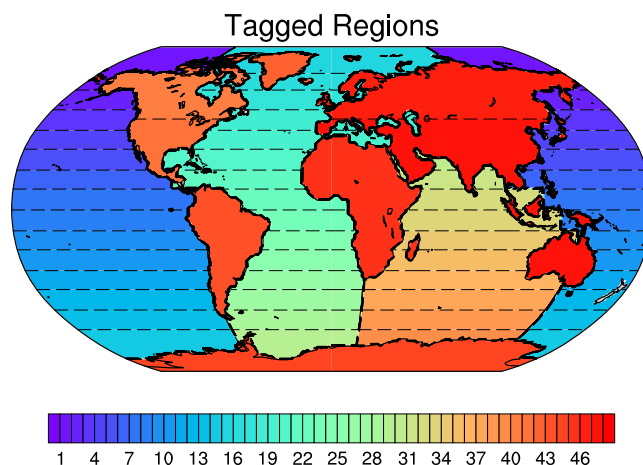
Tagged Regions

Figure 1. The 39 ocean regions and 9 land regions from which evaporated water is tagged. Each ocean basin is tagged separately in 10° latitude bands, with exceptions as noted in Table 2. Each major land mass (including Greenland) has its own tag, with North America and Eurasia subdivided at 45°N to have two tags each; for more details, see Table 3.

4. Results

The annually and seasonally averaged precipitation and evaporation fields in the model (Figure 2) reveal the importance of moisture divergence and convergence in determining the spatial pattern of precipitation. In general, evaporation depends on the availability of energy at the surface and varies smoothly with latitude, with a local minima over the deep tropics (where high relative humidity and cloud cover suppress evaporation), smooth maxima over the subtropics, and gradually decreasing toward the poles. The precipitation field, on the other hand, displays a finer spatial structure than the evaporation field, with a sharp global

Table 2. Description of Each Tagged Ocean Region, Designated by Ocean Basin (Pacific, Atlantic, and Indian) and Latitude Band[a]

Tracer	Basin	Latitude Band	Notes
NH75P	Pacific	90°N–60°N	Pacific Arctic; 100°E–260°E
NH55P	Pacific	60°N–50°N	
NH45P	Pacific	50°N–40°N	
NH35P	Pacific	40°N–30°N	
NH25P	Pacific	30°N–20°N	
NH15P	Pacific	20°N–10°N	
NH05P	Pacific	10°N–Eq	
SH05P	Pacific	Eq–10°S	
SH15P	Pacific	10°S–20°S	
SH25P	Pacific	20°S–30°S	
SH35P	Pacific	30°S–40°S	
SH45P	Pacific	40°S–50°S	
SH55P	Pacific	50°S–60°S	Pacific portion of Southern Ocean; 140°E–290°E
SH65P	Pacific	60°S–90°S	Pacific portion of Southern Ocean; 140°E–290°E
NH80A	Atlantic	90°N–70°N	Atlantic Arctic; 100°W–100°E
NH65A	Atlantic	70°N–60°N	
NH55A	Atlantic	60°N–50°N	
NH45A	Atlantic	50°N–40°N	
NH35A	Atlantic	40°N–30°N	
NH25A	Atlantic	30°N–20°N	
NH15A	Atlantic	20°N–10°N	
NH05A	Atlantic	10°N–Eq	
SH05A	Atlantic	Eq–10°S	
SH15A	Atlantic	10°S–20°S	
SH25A	Atlantic	20°S–30°S	
SH35A	Atlantic	30°S–40°S	
SH45A	Atlantic	40°S–50°S	
SH55A	Atlantic	50°S–60°S	Atlantic portion of Southern Ocean; 70°W–20°E
SH65A	Atlantic	60°S–90°S	Atlantic portion of Southern Ocean; 70°W–20°E
NH25I	Indian	30°N–20°N	
NH15I	Indian	20°N–10°N	
NH05I	Indian	10°N–Eq	
SH05I	Indian	Eq–10°S	
SH15I	Indian	10°S–20°S	
SH25I	Indian	20°S–30°S	
SH35I	Indian	30°S–40°S	
SH45I	Indian	40°S–50°S	
SH55I	Indian	50°S–60°S	Indian portion of Southern Ocean; 20°E–140°E
SH65I	Indian	60°S–90°S	Indian portion of Southern Ocean; 20°E–140°E

[a]Longitudinal limits are also included for regions in which the described tagged region is not confined to the specified ocean basin by land masses (i.e., regions that lie within the Arctic and Southern Ocean regions).

Table 3. Description of Each Tagged Land Region, Designated by Continent and Latitude Limits (if Applicable)

Tracer	Continent	Latitude Limits	Notes
NA45N	North America	North of 45°N	Does not include Greenland
NA45S	North America	South of 45°N	
GN	Greenland		
SA	South America		
AA	Antarctica		
AF	Africa		Includes Madagascar
EU45N	Eurasia	North of 45°N	
EU45S	Eurasia	South of 45°N	Includes the Maritime Continent
AU	Australia		Includes New Zealand

maximum near the equator, and local maxima over the storm tracks. Model biases are evident in the spatial distribution of P [see, i.e., *Yang et al.*, 2013; *Wehner et al.*, 2014; *Qian et al.*, 2015], particularly a prominent second precipitation maximum south of the equator over the Pacific basin in DJF; this double ITCZ problem is common to many global climate models, and may result from biases in tropical sea surface temperatures and associated cloud and radiative feedbacks [see *Lin*, 2007; *Liu et al.*, 2014; *Li and Xie*, 2014]. The difference between the E and P fields shows that moisture transport transforms the diffuse spatial pattern of evaporation into the sharp spatial pattern of precipitation.

Next, we show that these patterns of E and P are captured well when the model fields are averaged over the tagged regions. Over the ocean, the annual mean precipitation area averaged by tagged region, $\vec{P}$, (Figure 3a) captures the strong maximum at the Inter-Tropical Convergence Zone (ITCZ), minima at the subtropics (between 10°N and 30°, N and S), and weaker maxima at the midlatitude storm tracks (between 40° and 60°, N and S). The annual mean evaporation area averaged by tagged region, $\vec{E}$, (Figure 3d) has a bimodal structure in which $\vec{E}$ peaks in each of the subtropical regions; there is a local minimum at the equator and tails on each poleward side approaching zero. The seasonal changes in $\vec{E}$ and $\vec{P}$ include a slight shift in the position of the ITCZ away from the winter hemisphere (compare Figures 3b and 3c), a Hadley cell with a strongly evaporative subsiding region in the winter hemisphere (compare Figures 3e and 3f), and enhanced precipitation at the SH and NH storm tracks during their respective winters (compare Figures 3b and 3c).

While the spatial structure of $\vec{E}$, both annually and seasonally averaged, is similar for the three ocean basins, the spatial structure of $\vec{P}$ is less so. The Atlantic, in particular, receives the least precipitation per unit area despite large evaporative fluxes that rival those of the other ocean basins. The region between 30°N and 30°S in the Atlantic is especially dry (E – P is large and positive) relative to the same regions in the Indian and Pacific basins. The South Asian monsoon is also apparent in the seasonal precipitation patterns, with precipitation that is focused over the Maritime continent in DJF moving over the Indian subcontinent in
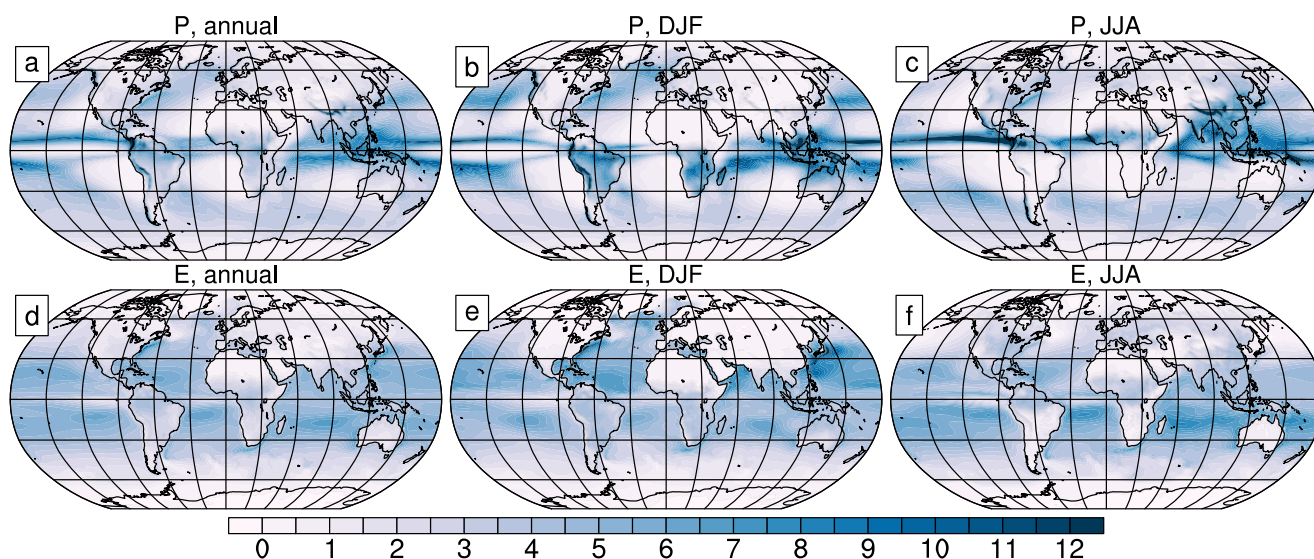
Figure 2. The (a–c) precipitation P and (d–f) evaporation E in the CESM1.2 preindustrial mean state, in mm d^{-1}. Quantities are shown in the (a, d) annual mean, (b, e) DJF, and (c, f) JJA.
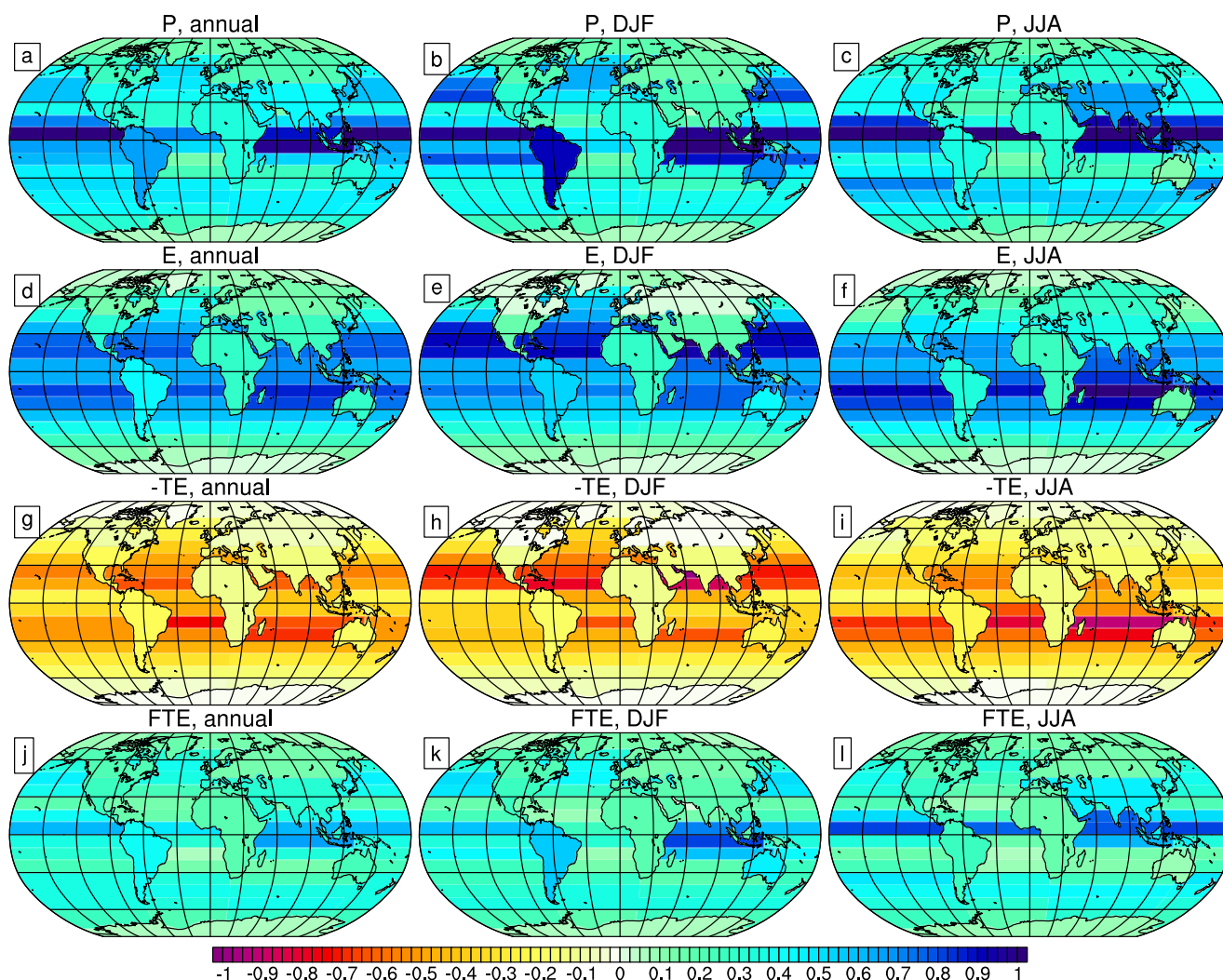
Figure 3. The (a–c) precipitation $\vec{P}$, (d–f) evaporation $\vec{E}$, (g–i) divergence of locally evaporated moisture $-\mathbf{T}\vec{E}$, and (j–l) convergence of remotely evaporated moisture $\mathbf{FT}\vec{E}$, as developed in equations (10) and (11). These terms are shown in the (a, d, g, j) annual mean, (b, e, h, k) for DJF, and (c, f, i, l) for JJA. All quantities are in normalized units of length per area, m^{-1}.

JJA. These basin-wide differences in precipitation and net $E - P$ are similar to those found in various observational data sets [see, e.g., *Bryan and Oort*, 1984; *Trenberth et al.*, 2011], and indicate that the hydrological cycle over the world oceans is simulated reasonably well by CESM1.2. These differences between basins are also apparent when averaged over the 48 tagged regions in our WT experiment.

4.1. The Structure of the Local Divergence Term, $-\mathbf{T}\vec{E}$

The term $-\mathbf{T}\vec{E}$ in equation (11) quantifies the divergence of locally evaporated moisture (Figures 3g–3i). $-\mathbf{T}\vec{E}$ exports away some fraction of the local evaporation, thereby decreasing the moisture available to precipitate locally. This exported fraction is then allocated to other regions by the $\mathbf{FT}\vec{E}$ term (Figures 3j–3l), which we consider in greater detail in section 4.3.

The spatial structure of $-\mathbf{T}\vec{E}$ is similar to that of the evaporation, and regions that are more evaporative, such as the subtropics, experience more moisture divergence than those regions that are less evaporative, such as the high latitudes. The exception to this rule is within the deep tropics (between 10°N and 10°S), where there is substantial evaporation but much of this locally evaporated moisture also precipitates locally.

The expression $\vec{E} - \mathbf{T}\vec{E}$, shown in Figure 4, represents the portion of the total precipitation that is due to locally evaporated moisture alone. For a given region i, this is $(1 - e_i)E_i$, equal to the total moisture
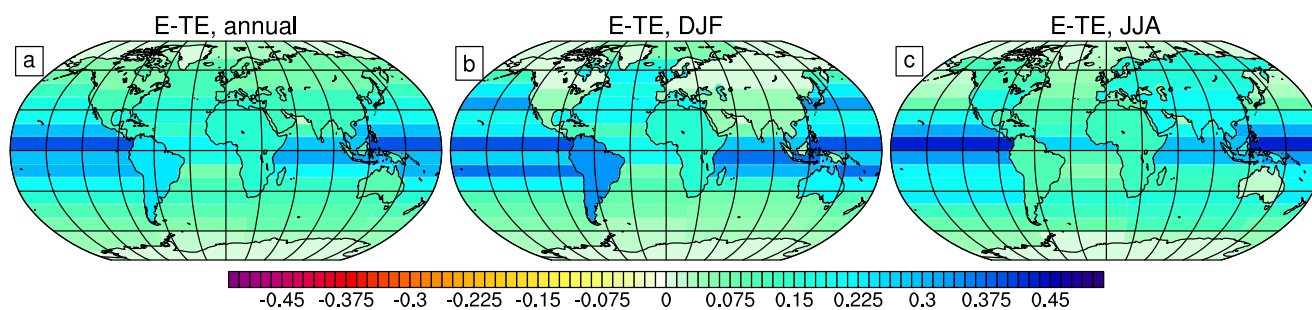
Figure 4. The sum of terms $\vec{E} - \mathbf{T}\vec{E} = (\mathbf{I} - \mathbf{T})\vec{E}$, which represents the locally evaporated moisture in each tagged region that is precipitated locally. Shown for the (a) annual mean, (b) DJF, and (c) JJA. All quantities are in normalized units of length per area, m^{-1}. Note that the colorbar differs from that used in Figure 3.

evaporated from the region, E_i, reduced by the portion that is exported, $e_i E_i$. In the annual mean (Figure 4a), this local contribution to the precipitation varies smoothly, with a broad maximum in the tropics. Seasonally, the local contribution includes a second, weaker maximum at the location of the midlatitude storm track in the winter hemisphere, especially in the NH (Figures 4b and 4c).

Comparing the ocean basins highlights regional asymmetries in the local divergence $-\mathbf{T}\vec{E}$ (Figures 3g–3i) and the local contribution to the total precipitation $\vec{E} - \mathbf{T}\vec{E}$ (Figure 4). The Atlantic basin has the highest local moisture divergence, particularly over the subtropics; as a result, the local contribution is also the smallest over the Atlantic compared to the local contributions over the Indian and Pacific basins. Over land areas, locally evaporated moisture is not very divergent, and each land region loses little locally evaporated moisture to adjacent areas. While this is hardly surprising given the large spatial areas that each land tag covers (recall Figure 1 and Table 3), other studies have also noted that moisture recycling (i.e., precipitation sourced from local evaporation) is particularly important over large land regions, especially for those that are sufficiently removed from ocean source regions [see *Eltahir and Bras*, 1996; *Trenberth*, 1999; *Gimeno et al.*, 2010; *Trenberth et al.*, 2011].

Figure 5 shows the fraction of locally evaporated moisture that precipitates remotely (e_i, the export fraction). While e_i, undoubtedly, depends on the size and geographic orientation of the domain over which it is computed (see Appendix A), it does provide a useful index for comparing the relative moisture divergence (and size of the local contribution) between tagged regions. In the annual average, the export fraction is large and surprisingly homogeneous over ocean domains ($e_i \approx 0.75$). The smallest e_i values are found in the deep tropics over the Pacific basin and over ice-covered regions in the Arctic and Antarctic; the largest values ($e_i \approx 1.0$) are found over the Atlantic basin subtropics, particularly south of the equator. Over ocean, the gross spatial structure of the export fraction agrees with our intuition of how the atmospheric circulation transports moisture: the export fraction is smallest where there is little divergence of moisture (at the equator and the poles), and largest in the subtropics (where the mean circulation diverges moisture equatorward and midlatitude eddies move moisture poleward).

The export fraction is more heterogeneous over land than ocean, though the large size of the tagged continental domains tends to mask this. Africa, Eurasia, and South America export less moisture than much of the surrounding ocean (0.5 for these land regions compared to 0.75 over ocean); the lower export fractions and higher evaporation recycling ratios over these regions are consistent with results from *van der Ent et al.* [2010]. Over some land areas, the export fraction varies dramatically by season: 0.3 in DJF compared to 0.65 in JJA for South America; and 0.8 in DJF compared to 0.4 in JJA for southern Eurasia; and 0.5 in DJF compared to 0.9 in JJA for Australia. Over others, particularly Africa, northern Eurasia, and North America, the export fraction remains relatively constant year round. For Greenland and Antarctica, the export fraction remains large year round ($e_i \approx 0.8$) due to large-scale subsidence and downslope flow over these elevated ice sheets that tend to advect locally evaporated (or locally sublimated) moisture away.

4.2. The Relative Contributions of Remotely and Locally Evaporated Moisture to the Precipitation

In Figure 6, we show $\mathbf{FT}\vec{E}/\vec{P}$, the fraction of the precipitation due to the convergence of remotely evaporated moisture (Figures 6a–6c), and its corollary $(\vec{E} - \mathbf{T}\vec{E})/\vec{P}$, the fraction of the precipitation due to *in situ* precipitation of locally evaporated moisture (Figure 6d–6f). First, we note that the former exceeds the latter

Export Fraction, annual

Export Fraction, DJF

Export Fraction, JJA
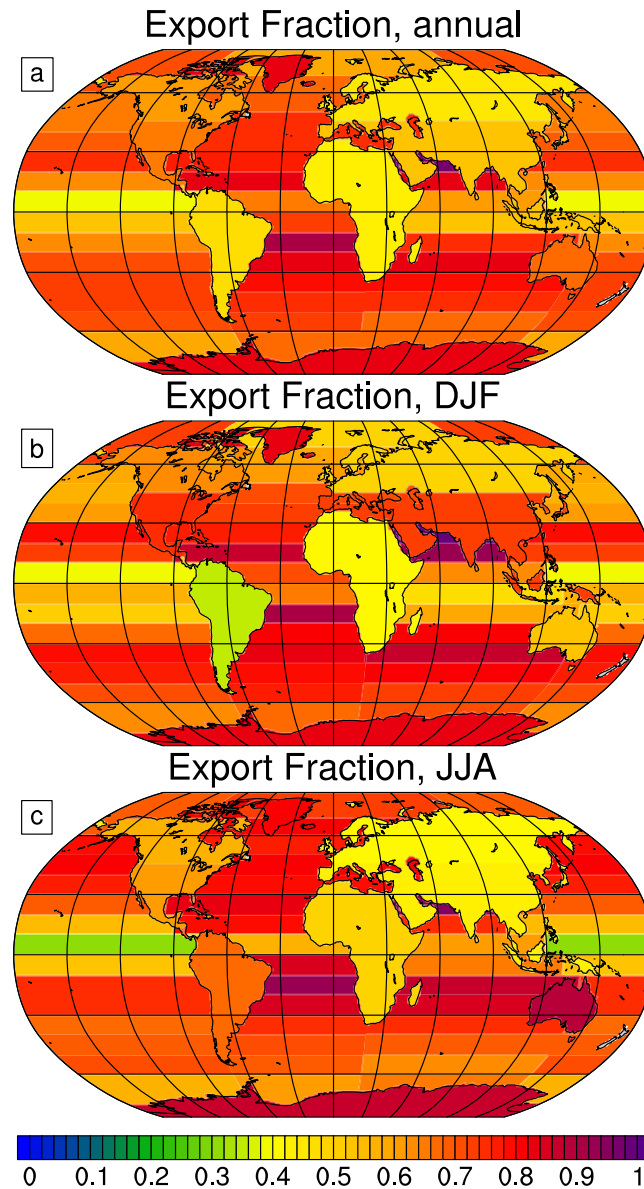
Figure 5. The export fraction e_i, the fraction of locally evaporated moisture that diverges and precipitates remotely, in the (a) annual mean, (b) for DJF, and (c) for JJA.

globally, except over the subtropics. An area-weighted average over all tagged regions yields $(\mathbf{FT}\vec{E}/\vec{P})_{global} \approx 0.7$. In Appendix A, we show that for a given region, $\mathbf{FT}\vec{E}/\vec{P}$ decreases logarithmically with area. Furthermore, we note striking regional differences in the relative contributions of locally and remotely evaporated moisture to the precipitation, as the remote (local) contribution becomes more (less) important to the total precipitation as one moves from equator to pole. The deep tropics are the exceptions to this general rule, as the remote contribution to the precipitation is more important here than in the neighboring subtropics.

Seasonal differences are also apparent. The NH (SH) subtropics rely most on the local contribution in DJF (JJA), consistent with greatest divergence of subtropical moisture by the Hadley circulation and eddies in the winter hemisphere. The remote contribution is more important over North America and Eurasia in DJF than in JJA, which is consistent with previous studies showing that local contributions are most important over large land masses in summer [*Numaguti*, 1999; *Bosilovich and Schubert*, 2002]. Over mid-latitude and high-latitude oceans, on the other hand, remote contributions to the precipitation are most important in the summer than winter, with this seasonality much more pronounced in the NH.

4.3. Decompositions of the Remote Moisture Convergence Term, $\mathbf{FT}\vec{E}$

To investigate the remote moisture convergence in greater detail, we decompose $\mathbf{F}$ into a finite sum of matrices $\mathbf{F}_p$ which we use to subdivide the remote convergence into p terms:

$$\mathbf{FT}\vec{E} = \sum_p \mathbf{F}_p \mathbf{T}\vec{E} = \sum_p \left(\mathbf{FT}\vec{E}\right)_p . \tag{15}$$

First, we decompose $\mathbf{F}$ into a set of submatrices depending on whether the areas of evaporation and precipitation are over ocean or land: (1) moisture that evaporates from the ocean also precipitates over the ocean, $\mathbf{F}_{OO}$; (2) moisture that evaporates from the ocean precipitates over land, $\mathbf{F}_{OL}$; (3) moisture that evaporates from land precipitates over the ocean, $\mathbf{F}_{LO}$; and (4) moisture evaporating from land also precipitates over land, $\mathbf{F}_{LL}$. Therefore, $\mathbf{F}$ is written as the sum

$$\mathbf{F} = \mathbf{F}_{OO} + \mathbf{F}_{OL} + \mathbf{F}_{LO} + \mathbf{F}_{LL} . \tag{16}$$

Substituting components of $\mathbf{F}$ from equation (16) into equation (15) yields the components of $\mathbf{FT}\vec{E}$ shown in Figure 7. Immediately apparent is that $\mathbf{F}_{OO}\mathbf{T}\vec{E}$, the portion of the remote convergence term due to

Figure 6. (a–c) The fraction of the precipitation due to the convergence of remotely evaporated moisture $\mathbf{FT}\vec{E}/\vec{P}$, and (d–f) the fraction of precipitation due to locally evaporated moisture precipitating in situ $(\vec{E}-\mathbf{T}\vec{E})/\vec{P}$. Values are shown for the (a, d) annual mean, (b, e) DJF, and (c, f) JJA.
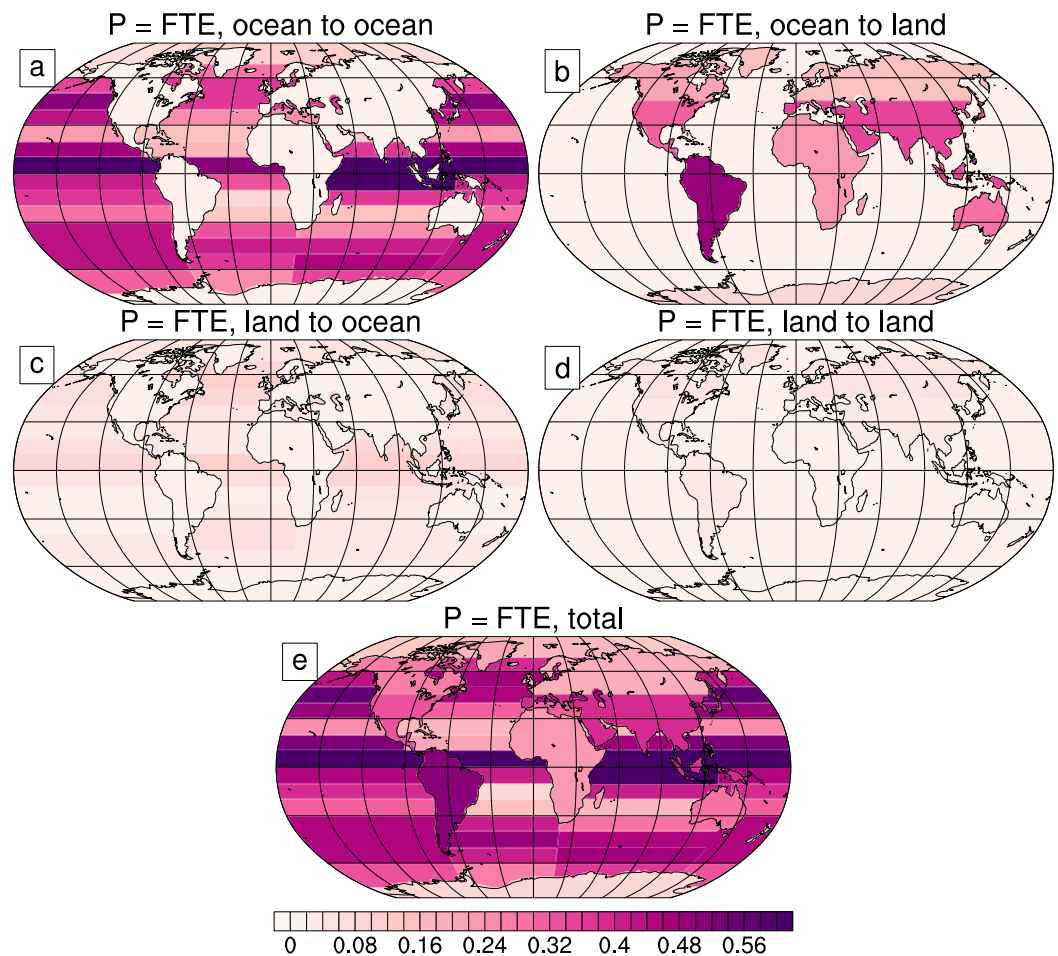
Figure 7. Physics-based decomposition of $\mathbf{FT}\vec{E}$ in the annual average. The top two rows show decomposition of the remote convergence term $\mathbf{FT}\vec{E}$ into components as described in equation (16): (a) ocean to ocean, (b) ocean to land, (c) land to ocean, and (d) land to land components. (e) The full $\mathbf{FT}\vec{E}$ term is also shown.

evaporation and precipitation over ocean (Figure 7a), is much greater in magnitude than $\mathbf{F}_{LO}\mathbf{T}\vec{E}$, the portion due to evaporation over land and precipitation over ocean (Figure 7c). Likewise, $\mathbf{F}_{OL}\mathbf{T}\vec{E}$, the portion of the remote convergence term due to evaporation from ocean and precipitation over land (Figure 7b), is much greater in magnitude than $\mathbf{F}_{LL}\mathbf{T}\vec{E}$, the portion of the remote convergence term due to evaporation and precipitation over land (Figure 7d). Neither of these results are surprising, given that evaporation over the world oceans greatly exceeds evaporation over land as it is not limited by surface moisture availability [*Trenberth et al.*, 2011]. In addition, each individual land tag covers a large geographic area, a feature of the experiment design that minimizes moisture transfer between tagged land regions. In the following analysis, the ocean-to-ocean term (Figure 7a) is further subdivided using physically motivated considerations; we consider the ocean-to-land term (Figure 7b) further in section 4.4.

We present three physical decompositions of matrix $\mathbf{F}_{OO}$. In the first, $\mathbf{F}_{OO}$ is subdivided three components: (1) where moisture precipitates north of its point of evaporation, $\mathbf{F}_{SN}$, (2) where moisture precipitates south of its point of evaporation, $\mathbf{F}_{NS}$, and (3) where moisture precipitates within the same latitude band (but different ocean basin) as where it evaporated, $\mathbf{F}_{zonal}$:

$$\mathbf{F}_{OO}=\mathbf{F}_{SN}+\mathbf{F}_{NS}+\mathbf{F}_{zonal} \quad . \tag{17}$$

In the second, $\mathbf{F}_{OO}$ is subdivided into an interbasin component $\mathbf{F}_{inter}$ (where moisture evaporates in one ocean basin and precipitates in another) and an intrabasin component $\mathbf{F}_{intra}$ (where moisture evaporates and precipitates in the same basin):

$$\mathbf{F}_{OO}=\mathbf{F}_{inter}+\mathbf{F}_{intra} \quad . \tag{18}$$

In the third, $\mathbf{F}_{OO}$ is subdivided three components: (1) a pure meridional part in which moisture travels meridionally within the basin in which it evaporated to its point of precipitation, $\mathbf{F}_{merid}$, (2) a pure zonal component in which moisture evaporates within a given latitude band and precipitates in the same latitude band but in a different basin, $\mathbf{F}_{zonal}$, and (3) a cross component in which moisture travels both meridionally and zonally from its region of evaporation to its region of precipitation, $\mathbf{F}_{cross}$:

$$\mathbf{F}_{OO}=\mathbf{F}_{merid}+\mathbf{F}_{zonal}+\mathbf{F}_{cross} \quad . \tag{19}$$

Applying equation (15) to each of these three decompositions yields the various components of the remote convergence term in the annual mean (Figure 8) and by season (Figure 9).

First, we consider the decomposition of $\mathbf{F}_{OO}$ given in equation (17). Figures 8a–8c show that for all basins, moisture converging into the midlatitude and subpolar oceans mostly originates equatorward of where it precipitates. Seasonal changes in this moisture convergence are apparent in Figure 9 (compare Figures 9a–9c with Figures 9i–9k). In the NH, there is a clear seasonality to moisture convergence, in that convergence is much stronger in DJF than it is in JJA (compare Figures 9b and 9j). In the SH, on the other hand, there is much less of a seasonal difference, though there is slightly less northerly moisture transport and convergence in DJF than in JJA (compare Figures 9a and 9i).

Unlike the midlatitude and high latitude, moisture convergence into the deep tropics has a distinct spatial and seasonal pattern that varies by basin. In the annual mean, moisture converging over the equatorial Indian ocean originates mostly from the south, which is expected due to the geographical constraints of the basin. The northward transport of latent heat in JJA by the Hadley circulation is responsible for most equatorward moisture transport in the Indian basin since there is not much ocean area available for evaporation in the NH subtropics. As a result, northerly moisture convergence over the equatorial Indian is modest in DJF (Figure 9a), while southerly moisture convergence is substantial in JJA (Figure 9j).

Over the Atlantic basin, equatorial precipitation tends to be dominated by southerly convergence by the Hadley circulation, though this seasonal difference in the atmospheric moisture transport is not due to obvious geographical constraints, as they are for the Indian basin. In the Pacific basin, on the other hand, both northerly and southerly moisture convergence by the Hadley circulation are responsible for creating the equatorial precipitation maximum (compare Figures 9a with 9j), with northerly (southerly) moisture transport dominating DJF (JJA) as expected.

Next, we consider the decomposition of $\mathbf{F}_{OO}$ given in equation (18), which separates the intrabasin and interbasin components of the moisture convergence. In general, the intrabasin moisture convergence
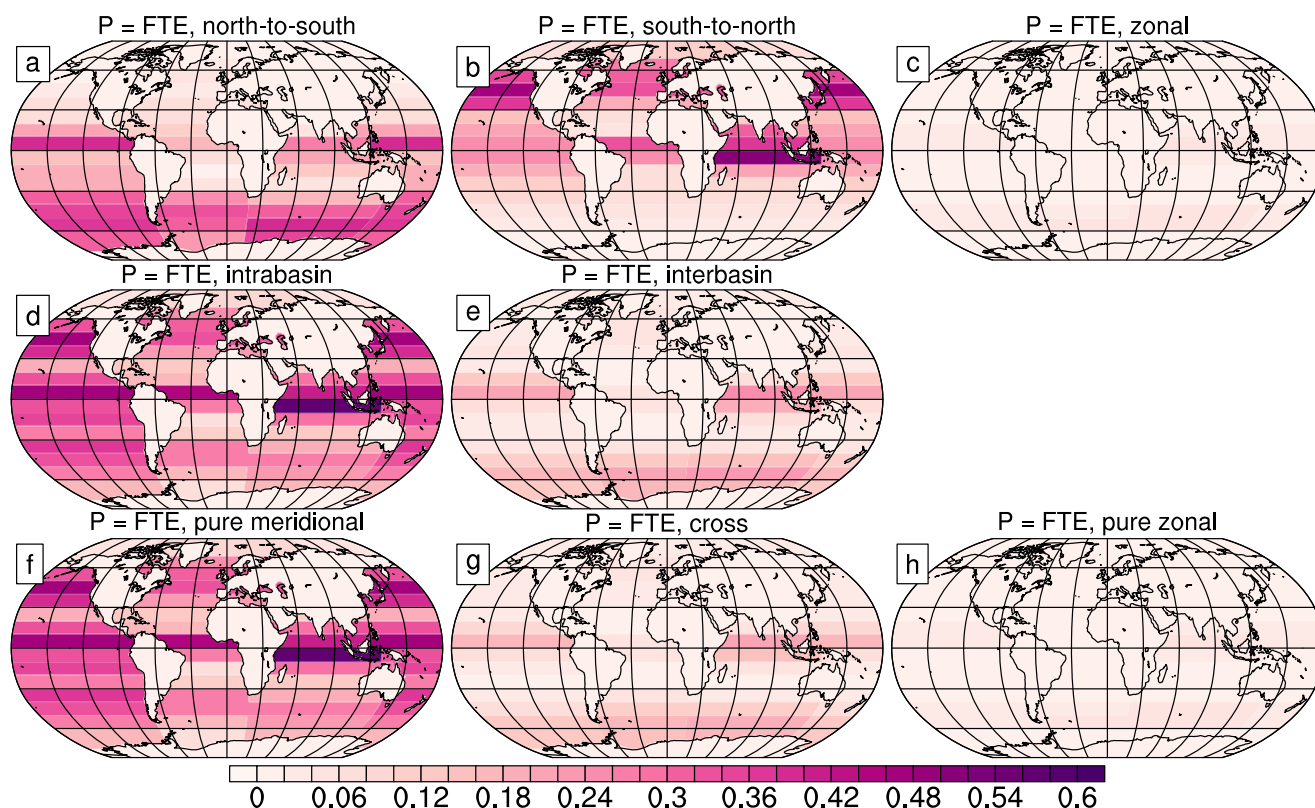
Figure 8. Physics-based decomposition of $\mathbf{F}_{OO}\mathbf{T}\vec{E}$ in the annual average. The top row shows decomposition into (a) northward, (b) southward, and (c) zonal components, as in equation (17); the middle row shows decomposition into (d) intrabasin and (e) interbasin components, as in equation (18); and the bottom row shows decomposition into (f) a purely meridional component, (g) a cross component (both meridional and zonal), and (h) a purely zonal component, as in equation (19). As described in the text, each row sums to the total ocean-to-ocean convergence term, $\mathbf{F}_{OO}\mathbf{T}\vec{E}$.

greatly exceeds the interbasin contribution (compare Figure 8d with Figure 8e, Figure 9d with Figure 9e, and Figure 9l with Figure 9m). Given that distance and orography separate the ocean basins at most latitudes, it is not surprising that intrabasin convergence greatly exceeds interbasin convergence.

There are, however, a few regions where interbasin moisture transport is significant. Over the equatorial Pacific and Indian basins, interbasin moisture convergence is significant year round (see Figures 8e, 9e, and 9m), with larger interbasin moisture convergence over the equatorial Pacific (Indian) in JJA (DJF). In the tropics, equatorial easterlies advect moisture westward; when land distances are sufficiently small and orography is low, these winds can transport moisture between basins. Thus, moisture evaporated from the Atlantic basin can travel over the Isthmus of Panama to precipitate over the Pacific, and moisture evaporated from the Pacific basin can travel over the Maritime continent to precipitate over the Indian. On the other hand, the African continent is too great a land barrier, and little moisture is transported from the Indian basin to the Atlantic. Over the Southern Ocean (south of 50°S), the relative absence of land and orographic barriers allows for significant interbasin moisture convergence year round. Here, surface westerlies freely advect evaporated moisture eastward, and midlatitude eddies in the stormtrack also transport moisture poleward. In the NH storm track, conversely, there is little transport of moisture across basins due to blocking by the North American and Eurasian continents.

Finally, we may further decompose interbasin moisture convergence by using equation (19). The first term in this decomposition corresponds to the intrabasin moisture convergence, while the latter two sum to the interbasin moisture convergence. These latter terms allow the interbasin component to be separated further into a purely zonal part (where moisture evaporates from and precipitates in the same latitude band) and a cross part (where moisture evaporates from a different latitude band than the one it precipitates in). Overall, the purely zonal component is very small (see Figures 8h, 9h, and 9p), and most of the interbasin convergence is encompassed in the cross term (see Figures 8g, 9g, and 9o). This suggests that over all
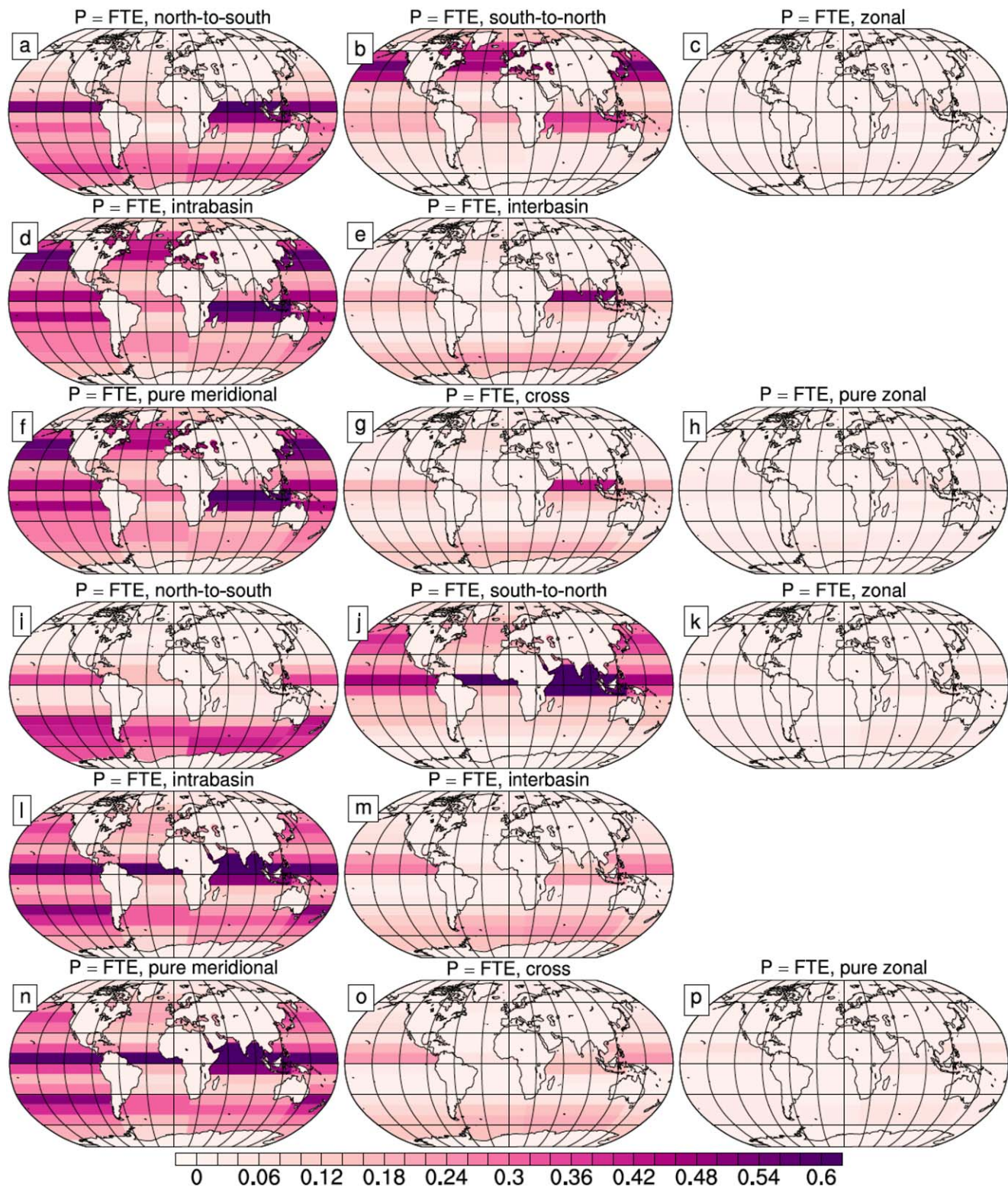
Figure 9. Physics-based decomposition of $\mathbf{FT}\vec{E}$ for (a–h) DJF and for (i–p) JJA. The decompositions are the same as described for Figure 8.

regions where interbasin moisture transport is important (i.e., in the tropics and over the Southern Ocean), this transport nearly always has a meridional component. Thus, both zonal and meridional advection are required to precipitate moisture in a basin that is different from its basin of origin.
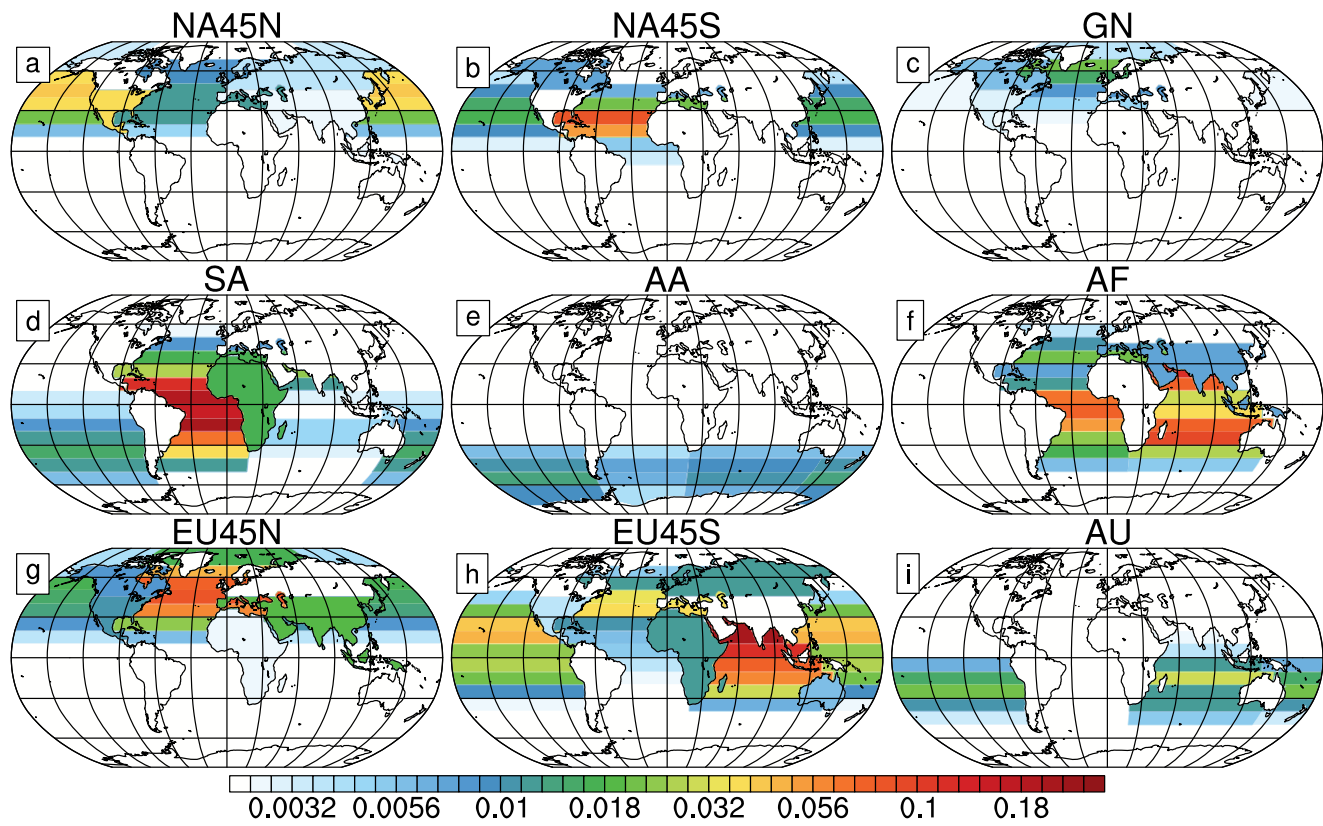
Figure 10. Sources of precipitation from remote regions $\tilde{E}_{ji}$, annually averaged and in normalized units of length per unit area of source region, for each of the tagged land areas: (a) North America, north of 45°N; (b) North America, south of 45°N; (c) Greenland; (d) South America; (e) Antarctica; (f) Africa; (g) Eurasia, north of 45°N; (h) Eurasia, south of 45°N; and (i) Australia. Note that the color bar is shown on a log scale.

4.4. Identifying Precipitation Source Regions Using FT$\vec{E}$

How much precipitation over a region is remotely sourced from every other tagged region? While **FT**$\vec{E}$ gives the total precipitation that originates remotely, it does not provide any information on which tagged regions this precipitation came from. Remote source regions are particularly interesting over land since a substantial fraction of terrestrial precipitation originates from the global ocean [*Trenberth et al.*, 2011; *Gimeno et al.*, 2012].

To visualize remote moisture convergence into one particular region, we consider individual terms in the product of matrices **FT** with $\vec{E}$. Consider the product of the *i*th row of **FT** with $\vec{E}$. This is the sum

$$\sum_{j,j\neq i} f_{ji}e_j E_j = \sum_{j,j\neq i} \tilde{E}_{ji} \quad , \tag{20}$$

where each $\tilde{E}_{ji}$ represents the part of the precipitation over region *i* that originated in region *j*. The sum of the $\tilde{E}_{ji}$ yields the portion of the total precipitation over region *i* that originated remotely, P_i^r:

$$\sum_{j,j\neq i} \tilde{E}_{ji} = P_i^r \quad . \tag{21}$$

The individual precipitation contributions $\tilde{E}_{ji}$ to each tagged land area *i* from all other tagged areas *j* is shown for the annual mean in Figure 10 and by season in Figure 11. Predictably, in the annual average and seasonally, ocean areas provide moisture to land areas that are down-wind. Thus, land regions in the tropics receive moisture from ocean that is to the east (via the equatorial easterly winds), while land regions in the midlatitudes receive moisture from ocean that is to the west (via the midlatitude westerly winds). Midlatitude cyclones transport moisture poleward to high-latitude regions, such as Greenland, northern Eurasia, northern North America, and Antarctica. Almost all of this moisture originates poleward of 30°N or 30°S, and very little moisture from the deep tropics precipitates in these midlatitude and high-latitude regions.
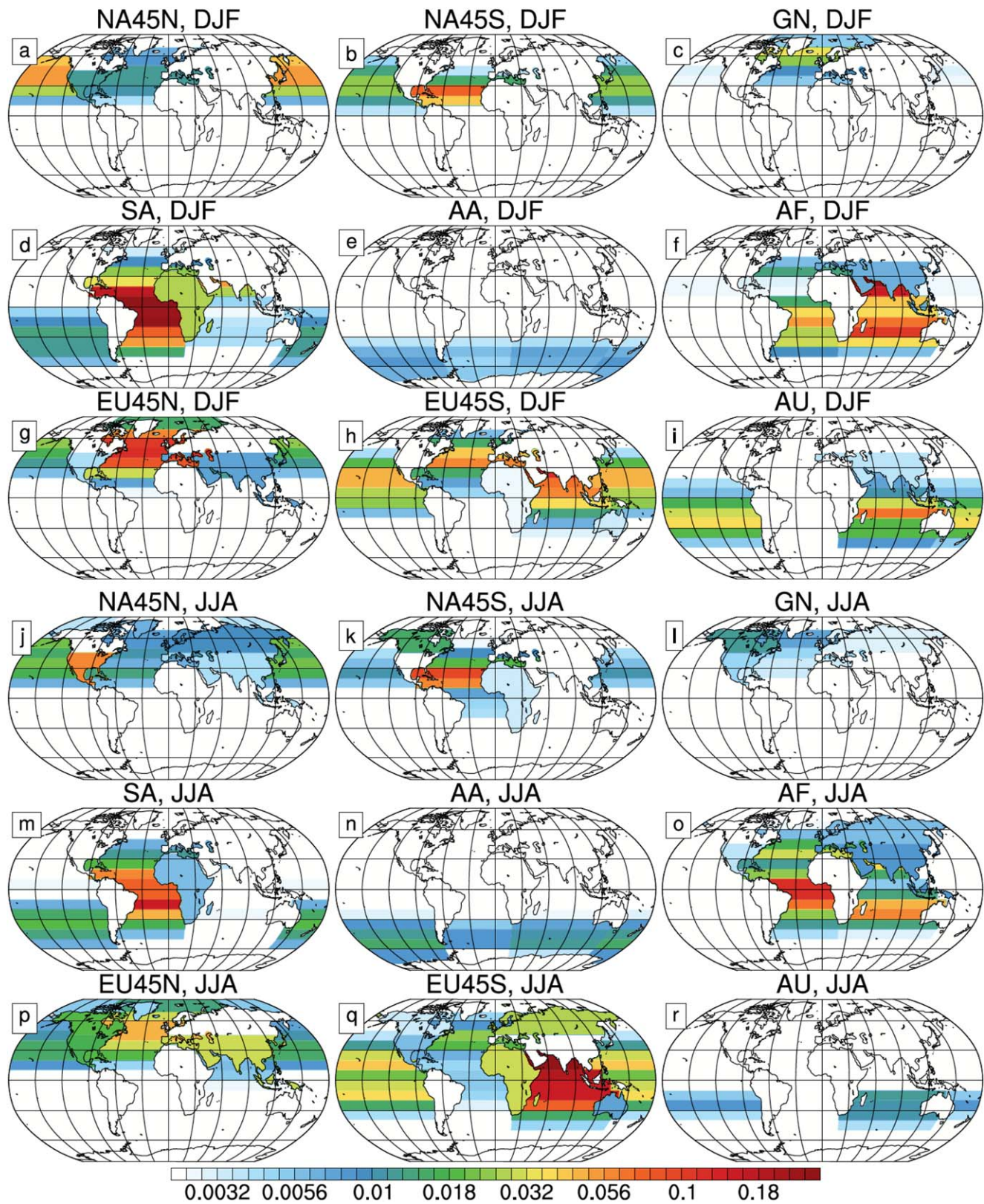
Figure 11. As in Figure 10, but for (a–i) DJF and (j–r) JJA.
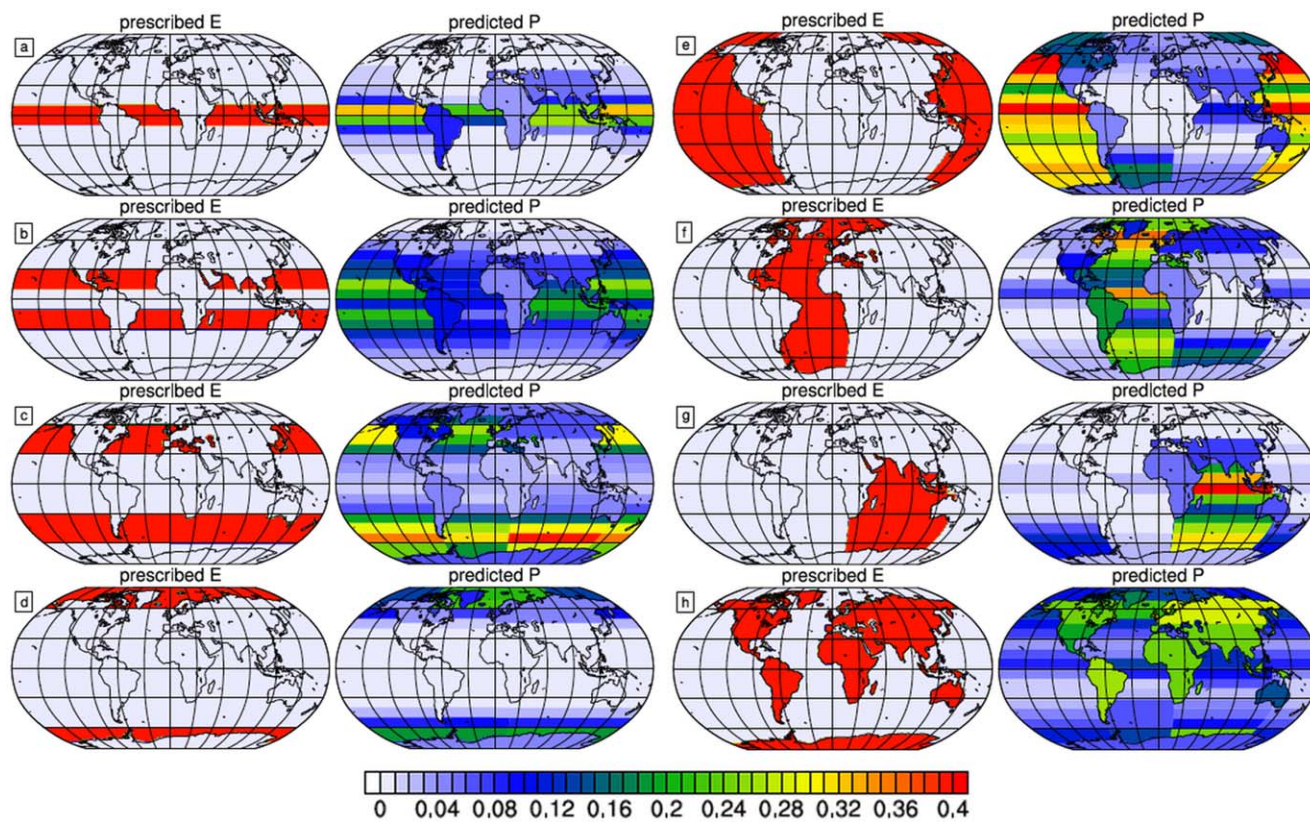
Figure 12. Predicted precipitation patterns corresponding to prescribed evaporation patterns. The predicted precipitation $\vec{P}$ is computed from substituting the prescribed evaporation $\vec{E}$ in equation (23). Prescribed evaporation regions in each plot are as follows: (a) equatorial, 10°N–10°S; (b) subtropics, 10°N–30°N and 10°S–30°S; (c) midlatitudes, 30°N–60°N and 30°S–60°S; (d) subpolar and polar, poleward of 60°N and 60°S; (e) the Pacific basin; (f) the Atlantic basin; (g) the Indian basin; and (h) all land regions. All quantities are in normalized units of length per area, m^{-1}.

Figures 10 and 11 both reveal substantial differences in the amount of moisture each ocean basin contributes to terrestrial precipitation. Year round, the Atlantic basin contributes the most moisture (per unit area) to precipitation over southern North America, Greenland, South America, and northern Eurasia; the importance of the subtropical Atlantic as a continental moisture source has been noted in previous studies [see, i.e., *Gimeno et al.*, 2010]. The Atlantic basin is also the most important source of precipitation for Africa in JJA, though the Indian basin dominates in the annual average and in DJF. In addition to Africa, the Indian basin is also the most important moisture source region for southern Eurasia and Australia. Surprisingly, the Pacific basin is the dominant moisture source for only two regions, northern North America and Antarctica. The Pacific basin, however, is an important moisture source for northern and southern Eurasia, southern North America, South America, and Australia, albeit a less important one than the other basins noted earlier.

4.5. Forward Methods Using the Operator M

Recall that the matrix operator $\mathbf{M} : \vec{E} \rightarrow \vec{P}$, which operates on some spatial pattern of evaporation to create some unique spatial pattern of precipitation, is defined as

$$\mathbf{M} = \mathbf{I} - (\mathbf{I} - \mathbf{F})\mathbf{T} \ , \tag{22}$$

and the evaporation and precipitation are related by $\mathbf{M}$ as

$$\mathbf{M}\vec{E} = \vec{P} \ . \tag{23}$$

Matrix $\mathbf{M}$ is area preserving (see Appendix B), and is a function of the climate state. Equation (23) may be used to compute the associated precipitation pattern $\vec{P}$ given any spatial evaporation pattern $\vec{E}$. We refer to this use of $\mathbf{M}$ as a forward calculation.
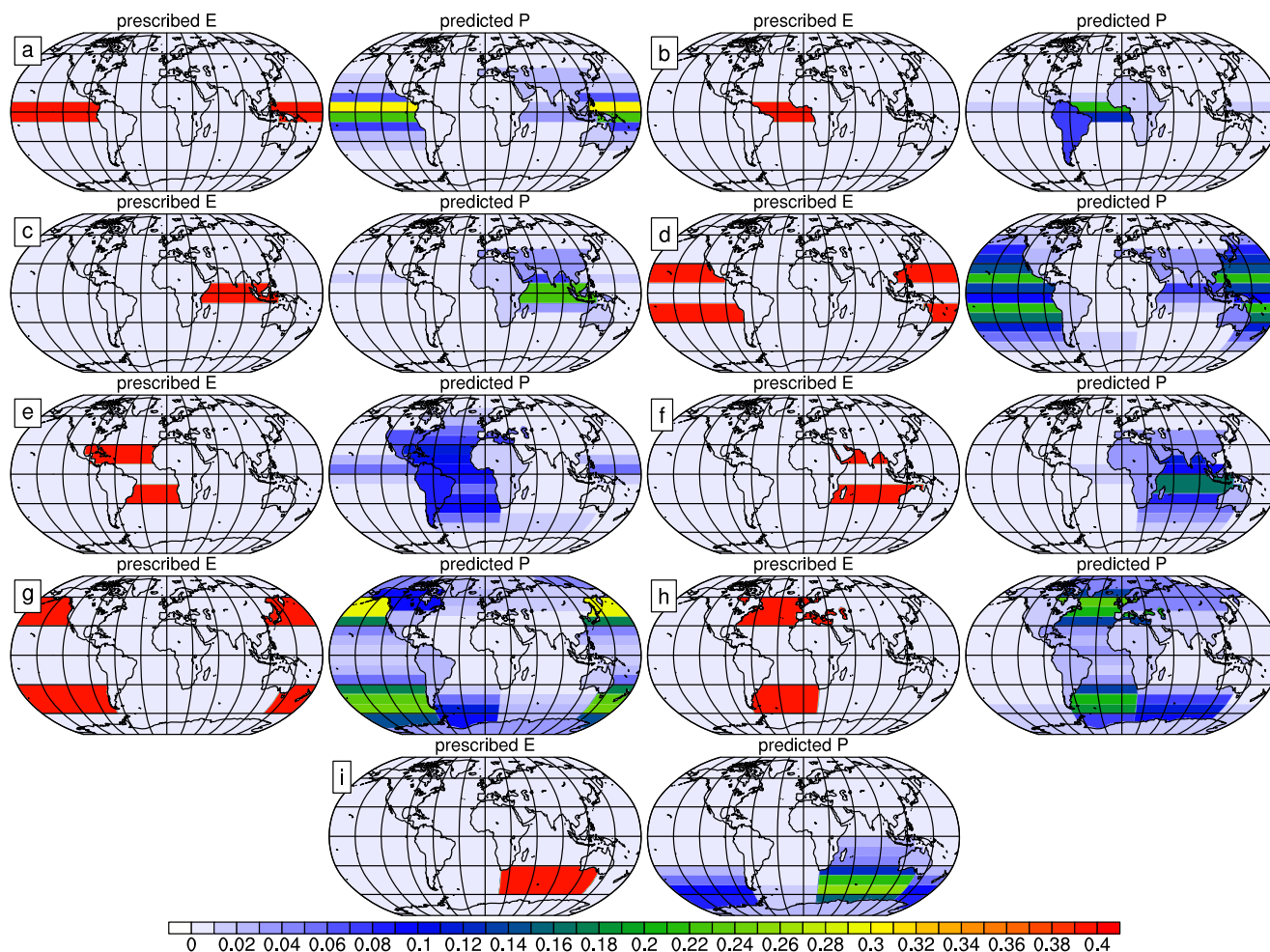
Figure 13. As for Figure 12, but for prescribed localized evaporation patterns over ocean. Prescribed evaporation regions in each plot are as follows: (a) equatorial Pacific, (b) equatorial Atlantic, (c) equatorial Indian, (d) subtropical Pacific, (e) subtropical Atlantic, (f) subtropical Indian, (g) midlatitude Pacific, (h) midlatitude Atlantic, and (i) midlatitude Indian.

Figures 12 and 13 show various prescribed spatial patterns of evaporation $\vec{E}$ and corresponding patterns of precipitation $\vec{P}$ computed using equation (23). The matrix **M** used is that computed from the annual-mean model output.

When $\vec{E}$ is prescribed in distinct latitudinal bands (Figures 12a–12d), it is clear that moisture evaporated in the deep tropics and high-latitudes tends to precipitate locally, while moisture evaporated in the subtropics and midlatitudes tends to precipitate remotely. Moisture that evaporates in the deep tropics remains mostly within this region (Figure 12a) because the lower branch of the Hadley circulation converges here. In contrast, moisture evaporated from regions where there is net divergence, such as the subtropics (Figure 12b), mostly precipitates outside its source region. Generally, moisture that evaporates from the subtropics travels either equatorward or poleward before precipitating. The lower limb of the Hadley circulation transports moist subtropical air toward the ITCZ while poleward moisture transport is accomplished by midlatitude eddies; the poleward-eastward slope of the midlatitude geopotential height field facilitates this transport.

In the midlatitudes, eddies transport locally evaporated moisture poleward (Figures 12c and 13g–13i). There is substantial hemispheric asymmetry in moisture transport from the midlatitude to high latitudes in that transport in the SH greatly exceeds transport in the NH in the annual mean. The Arctic (north of 60°N), in particular, receives little moisture from the NH midlatitude oceans, despite the fact that the majority of precipitation in the Arctic is remotely sourced (rather than local); the Antarctic (south of 60°S), on the other hand, receives a substantial amount of moisture from the SH midlatitudes, though precipitation over

Antarctica itself is small. This hemispheric asymmetry is partly due to the intervening land masses that surround the Arctic and intercept moisture from the midlatitude ocean; the absence of such obstacles in the SH allows greater meridional moisture transport in the Antarctic than the Arctic. Furthermore, there is more midlatitude ocean area in the SH so more moisture is available for poleward transport to the Antarctic than the Arctic. Unlike the subtropics, where a large fraction of locally evaporated moisture diverges and there is very little precipitation, a larger fraction of the moisture evaporated within the midlatitudes remains in the midlatitudes to precipitate within the storm tracks (compare Figures 12b and 12c).

When a spatially uniform evaporative flux is prescribed over an ocean basin (Figures 12e–12g), the resulting precipitation pattern has a strong maximum at the ITCZ and weaker maxima in the midlatitudes; there are corresponding precipitation minima in the subtropics. The midlatitude maxima are weakest over the Pacific basin since the subtropical minima are least pronounced here compared to the Indian and Atlantic basins. The reason for this becomes clear when precipitation resulting from evaporation in the Pacific subtropics is compared to that in the Indian and Atlantic subtropics (Figures 13d–13f): given a uniform surface evaporation per unit area, the most pronounced subtropical precipitation minimum is found in the South Atlantic, with the North Atlantic and South Indian subtropics following closely behind. The Pacific subtropics, on the other hand, are distinct in that they retain significant precipitation maxima (Figure 13d). Indeed, the Pacific subtropics provide much less precipitable water (per unit area) to surrounding land masses than the Atlantic and Indian subtropics.

Evaporation patterns confined to a particular basin also help pinpoint where moisture moving between basins comes from. As noted earlier, all basins "leak" moisture into adjacent basins, particularly when the distance between basins is short and intervening orography is low. This is true over the Southern Ocean, where the absence of land barriers allows evaporated moisture to move eastward freely in the midlatitude storm tracks. At the equator, however, interbasin moisture convergence is not uniform across basins. The Pacific basin leaks moisture into the Indian basin and receives moisture from the Atlantic. The Atlantic, on the other hand, leaks moisture into the equatorial Pacific but does not receive any compensating moisture from the Indian basin (compare Figures 12f and 12g), which receives moisture evaporated from the Pacific basin but leaks little to the Atlantic. Comparing Figures 13b and 13e reveals that the Atlantic subtropics, not the deep tropics, are mostly responsible for the interbasin contribution to equatorial precipitation in the Pacific. The interbasin-sourced precipitation in the Indian basin is also (mostly) from the Pacific subtropics, not the deep tropics (compare Figures 13a and 13d).

5. Discussion and Conclusions

In this study, we have presented a new mathematical framework for linking precipitation and evaporation that exploits data made available by implementing numerical WTs in an AGCM. Our mathematical framework uses straightforward techniques from linear algebra and analysis, and allows us to assess how the divergence of locally evaporated moisture and convergence of remotely evaporated moisture each contribute to the precipitation. Within this framework, we have used matrix decomposition methods to gain further insight into how remotely evaporated moisture converges differentially to create the distinct spatial pattern of global precipitation. We have also used the results from our tagging experiment to define a matrix operator that can be used to compute how a given spatial pattern of evaporation maps to a unique spatial pattern of precipitation.

The mathematical development that we have presented here is, by no means, only relevant to numerical WTs. We envision that these techniques could also be used in other regional or AGCM tracer studies, such as those that tag dust, biogenic substances, sea spray, trace gases, or other climate-relevant or meteorologically relevant variables that have a spatially heterogeneous source-to-sink relationship. The utility of this framework lies in its simplicity and physical relevance. Being linear, all coefficients are simple to compute; being cast into a linear algebra framework, many powerful matrix decomposition methods may be used to analyze the results. Being able to separate the divergence of local sources from the convergence of remote sources allows both short-range and long-range influences to be evaluated. Allowing sinks to be predicted,

given a set of sources (and vice versa), offers a starting point for computing how each of these quantities evolves, given the other.

By applying our methods to the hydrological cycle in our model run, we have confirmed old insights and gained new insights on how moisture moves from local and remote sources of precipitation. These findings can be summarized in the following major points:

1. At 10° meridional spatial scales, the contribution of remotely evaporated moisture to the total precipitation over the world ocean is more important than the contribution of locally evaporated moisture. This is very evident in the high latitude and midlatitude, and less so in the tropics and subtropics. The distinct spatial pattern of precipitation mostly arises from the convergence of remotely evaporated moisture, not the locally evaporated moisture that precipitates in situ.
2. Interbasin contributions to precipitation are small, except over the Southern Ocean (where there are no land barriers to zonal flow), across the Isthmus of Panama, and across the Maritime continent.
3. Moisture evaporated in the high latitudes and deep tropics tends to precipitate in situ. In contrast, the general circulation transports moisture evaporated in the subtropics both equatorward and poleward and transports moisture evaporated in the midlatitudes poleward.
4. The Atlantic basin is unique in several ways: the Atlantic subtropics are the most divergent, as far as locally evaporated moisture is concerned; the Atlantic basin provides precipitable water to the largest land area; little remotely evaporated moisture converges over the Atlantic basin; the ITCZ over the Atlantic is very weak in DJF, with little north-to-south remote moisture convergence compared to that over the Pacific and Indian basins; and the Atlantic loses a significant amount of (subtropical) moisture to the equatorial Pacific, but does not regain any of this lost moisture from either the Pacific or Indian basins.

One interesting insight from this work is that remote evaporation contributes more to the precipitation at a given locale than local evaporation, even at 10° meridional spatial scales. We have shown that the contribution of the local evaporation to the total precipitation is, on average, about one third. This result agrees with that of other studies that have considered various land areas and their precipitation source regions [see *Numaguti*, 1999; *Bosilovich*, 2002; *Bosilovich and Schubert*, 2002; *Stohl and James*, 2009; *Gimeno et al.*, 2010]. While land-locked regions in the centers of the large continents (i.e., Eurasia, North America, and Africa) depend largely on this local contribution, particularly in the summer season, most other regions receive much of their locally precipitating moisture from a variety of remote source regions [*Gimeno et al.*, 2010, 2012].

In general, our results show that the distinct spatial pattern of precipitation is created by the convergence of remotely evaporated moisture which is made possible by atmospheric motions, not by in situ evaporation. Our results also show that each of the ocean basins exhibits distinct tendencies in where evaporated moisture travels before it precipitates. The Atlantic basin is the most divergent (in terms of locally evaporated moisture) and least convergent (in terms of remotely evaporated moisture); in contrast, the Pacific basin is the least divergent and most convergent. The Indian basin is set apart by the South Asian monsoon, whose seasonal movements are made possible by the sizeable subtropical land mass at its northern flank.

Finally, we point out the major caveat associated with this study and its findings: while numerical WTs may be a powerful tool, they are also a highly model-dependent one. It is likely that some of our results are specific to the aerial water advection, diffusion, and condensation schemes in CAM5, and to all model biases in E and P. While CESM 1.2 produces the spatial patterns of E and P over the world oceans relatively favorably (see the climatologies of freshwater input into the world oceans compiled by *Bryan and Oort* [1984] and *Ganachaud and Wunsch* [2003]; also see *Trenberth, et al.* [2011]), there are still substantial differences between the modeled hydrological cycle and that in the real world, particularly in the tropics. Determining which, if any, of our results are robust will depend on future work, in which we apply the mathematical methods presented here to results from several different models. Alternatively, we may also use numerical WTs in a data assimilation framework, and an AGCM equipped with numerical WTs may be used in conjunction with observational hydrological data. Such a study would allow us to evaluate how well AGCMs can capture evaporation, precipitation, and moist processes in the aerial hydrological cycle, and could provide some clues on how the hydrological cycle is changing in response to anthropogenic perturbations.

Appendix A: Area Dependence of Local and Remote Contributions to the Precipitation

Here we show that the RR decreases approximately linearly with the logarithm of domain area. This is consistent with earlier work where the scale dependence of the recycling ratio has been computed from observational data [see, e.g., *Eltahir and Bras*, 1996; *Brubaker et al.*, 2001; *Dirmeyer and Brubaker*, 2007].

For a region i, the fraction of the precipitation that is locally sourced (the RR) may be written as

$$RR_i = \frac{(1-e_i)E_i}{P_i} \quad . \tag{A1}$$

The local contribution L_i to the precipitation is

$$L_i = (1-e_i)E_i \quad , \tag{A2}$$

and the remote contribution R_i is

$$R_i = \sum_j e_j f_{ji} E_j. \tag{A3}$$

Now, suppose that the area of the domain i is halved. Assume that the two resulting spatial domains, $i/2$, each with half the area of the original domain, are sufficiently similar to each other so that $2E_{i/2}=E_i$ and $2P_{i/2}=P_i$. In this case, the local contribution to the precipitation is

$$L_{i/2} = \frac{1}{2}(1-e_{i/2})E_i \quad . \tag{A4}$$

The remote contribution is

$$R_{i/2} = \frac{1}{2}\sum_j f_{ij} e_j E_j + \frac{1}{2} f_x e_{i/2} E_i, \tag{A5}$$

where f_x is the fraction of exported moisture from the first subdivided region that falls in the second subdivided region, which we refer to as the exchange fraction.

The precipitation in the original region must be equal to the sum of the precipitation in the two subregions so that

$$L_i + R_i = 2(L_{i/2} + R_{i/2}) \quad . \tag{A6}$$

Substituting equations (A2)–(A5) and rearranging, we find that the export fraction in each divided region is related to the export fraction in the original domain by the exchange fraction:

$$e_{i/2} = \frac{e_i}{1-f_x}. \tag{A7}$$

Equation (A7) can be used to write equation (A4) as

$$L_{i/2} = \frac{1}{2}L_i - \frac{1}{2}f_x e_i E_i \quad . \tag{A8}$$

Now, we consider the recycling ratio for a subregion $i/2$. Using equation (A8) and simplifying, we find that

$$RR_{i/2} = \frac{L_i - e_i f_x E_i}{P_i} \quad . \tag{A9}$$

The change in the RR may be written as

$$RR_{i/2} - RR_i = -\frac{e_i f_x E_i}{P_i} \quad . \tag{A10}$$

Similarly, if the $i/2$ subregions are halved again to $i/4$, the local contribution to the precipitation is

$$L_{i/4} = \frac{1}{4}L_i - \frac{1}{4}e_i f_x E_i - \frac{e_i f_x E_i}{4(1-f_x)} \quad , \tag{A11}$$

which may be approximated by a (truncated) Taylor series expansion of the final term as

$$L_{i/4} \approx \frac{1}{4} L_i - \frac{1}{2} e_i f_x E_i - \frac{1}{4} e_i f_x^2 E_i \ . \tag{A12}$$

Dropping the f_x^2 term because it is small, the recycling ratio is

$$RR_{i/4} \approx \frac{L_i - 2e_i f_x E_i}{P_i} \ . \tag{A13}$$

Once again, we find that the change in RR with halfing of region area is

$$RR_{i/4} - RR_{i/2} \approx -\frac{e_i f_x E_i}{P_i} \ . \tag{A14}$$

Therefore, the change in the RR with halving of domain area results in an RR decrease of $e_i f_x E_i / P_i$. In other words,

$$\frac{\partial (RR)}{\partial (\log \text{area})} \sim \text{constant} \ , \tag{A15}$$

confirming a roughly log linear relationship between domain area and the RR. By extension, the fraction of the precipitation due to remotely evaporated moisture, $1 - RR$, must also scale similarly with domain area.

Appendix B: M is Area Preserving

We show that matrix **M** is area preserving by noting that the sum of all the entries of $\vec{E}$ must equal the sum of all the entries of $\vec{P}$, i.e.,

$$||\vec{E}||_1 = ||\vec{P}||_1 \ . \tag{B1}$$

This is merely a statement of the conservation of atmospheric water in a global sense, as expressed in equation (4). Thus, we may write the induced operator 1-norm of **M** as

$$||\mathbf{M}||_1 = \sup_{\vec{E} \neq 0} \frac{||\mathbf{M}\vec{E}||_1}{||\vec{P}||_1} = 1 \ , \tag{B2}$$

from which it follows that **M** must be area preserving since

$$\text{del } (\mathbf{M}) = 1. \tag{B3}$$

References

Bosilovich, M. (2002), On the vertical distribution of local and remote sources of water for precipitation, *Meteorol. Atmos. Phys.*, *80*, 31–41.

Bosilovich, M., and S. Schubert (2002), Water vapor tracers as diagnostics of the regional hydrologic cycle, *J. Hydrometeorol.*, *3*, 149–165.

Brown, D., J. Worden, and D. Noone (2012), Characteristics of tropical and subtropical atmospheric moistening derived from Lagrangian mass balance constrained by measurements of HDO and H$_2$O, *J. Geophys. Res. Atmos.*, *118*, 54–72, doi:10.1029/2012JD018507.

Brubaker, K., D. Entekhabi, and P. Eagleson (1993), Estimation of continental precipitation recycling, *J. Clim.*, *6*, 1077–1089.

Brubaker, K., P. Dirmeyer, A. Sudradjat, B. Levy, and F. Bernal (2001), A 36-yr climatological description of the evaporative sources of warm-season precipitation in the mississippi river basin, *J. Hydrometeorol.*, *2*(6), 537–557.

Bryan, F., and A. Oort (1984), Seasonal variation of the global water balance based on aerological data, *J. Geophys. Res.*, *89*(D7), 11,717–11,730.

Danabasoglu, G., S. Bates, B. Briegleb, S. Jayne, M. Jochum, W. Large, S. Peacock, and S. Yeager (2012), The CCSM4 ocean component, *J. Clim.*, *25*, 1361–1389.

Delaygue, G., V. Mason, J. Jouzel, R. Koster, and R. Healy (2000), The origin of Antarctic precipitation: A modelling approach, *Tellus, Ser. B*, *51*(1), 19–36.

Dirmeyer, P., and K. Brubaker (2007), Characterization of the global hydrologic cycle from back-trajectory analysis of atmospheric water vapor, *J. Hydrometeorol.*, *8*, 20–37.

Eltahir, E., and R. Bras (1996), Precipitation recycling, *Rev. Geophys.*, *34*(3), 367–378.

Ganachaud, A., and C. Wunsch (2003), Large-scale ocean heat and freshwater transports during the world ocean circulation experiment, *J. Clim.*, *16*, 696–705.

Gent, P., and J. McWilliams (1992), Isopycnal mixing in ocean circulation models, *J. Phys. Oceanogr.*, *20*, 150–155.

Gimeno, L., A. Drumond, R. Nieto, R. Trigo, and A. Stohl (2010), On the origin of continental precipitation, *Geophys. Res. Lett.*, *37*, L13804, doi:10.1029/2010GL043712.

Gimeno, L., A. Stohl, R. Trigo, F. Dominguez, K. Yoshimura, L. Yu, A. Drumond, A. Duran-Quesada, and R. Nieto (2012), Oceanic and terrestrial sources of continental precipitation, *Rev. Geophys.*, *50*, RG4003, doi:10.1029/2012RG000389.

Hartmann, D. (1994), *Global Physical Climatology, International Geophysics*, vol. 56, Academic, San Diego, Calif.

Hunke, E., and W. Lipscomb (2004), Cice: The Los Alamos sea ice model, documentation and software, version 3.1, *Tech. Rep. CC-98-16*, Los Alamos Natl. Laboratory, Los Alamos, NM, USA.

Hurrell, J., et al. (2013), The community earth system model: A framework for collaborative research, *Bull. Am. Meteorol. Soc.*, *94*, 1339–1360.

Joussaume, S., R. Sadourny, and C. Vignal (1986), Origin of precipitating water in a numerical simulation of July climate, *Ocean Air Interact.*, *1*, 43–56.

Knoche, H., and H. Kunstmann (2013), Tracking atmospheric water pathways by direct evaporation tagging: A case study for West Africa, *J. Geophys. Res. Atmos.*, *118*, 12,345–12,358, doi:10.1002/2013JD019976.

Koster, R., J. Jouzel, R. Suozzo, G. Russell, W. Broecker, D. Rind, and P. Eagleson (1986), Global sources of local precipitation as determined by the NASA/GISS GCM, *Geophys. Res. Lett.*, *13*(1), 121–124.

Koster, R., J. Jouzel, R. Suozzo, and G. Russell (1992), Origin of July Antarctic precipitation and its influence on deuterium content: A GCM analysis, *Clim. Dyn.*, *7*, 195–203.

Li, G., and S.-P. Xie (2014), Tropical biases in cmip5 multimodel ensemble: The excessive equatorial pacific cold tongue and double ITCZ problems, *J. Clim.*, *27*, 1765–1780.

Lin, J.-L. (2007), The double-ITCZ problem in IPCC ar4 coupled GCMS: Ocean-atmosphere feedback analysis, *J. Clim.*, *20*(18), 4497–4525.

Liu, Z., A. Mehran, T. Phillips, and A. AghaKouchak (2014), Seasonal and regional biases in cmip5 precipitation simulations, *Clim. Res.*, *60*, 35–50.

Neale, R., et al. (2012), Description of NCAR community atmosphere model (cam 5.0), NCAR/TN-486+STR, Boulder, Colo. [Available at: https://www.ccsm.ucar.edu/models/cesm1.0/cam/docs/description/cam5_desc.pdf.]

Noone, D., and I. Simmonds (2002), Annular variations in moisture transport mechanisms and the abundance of δ^{18} o in Antarctic snow, *J. Geophys. Res.*, *107*(D24), 4742, doi:10.1029/2002JD002262.

Numaguti, A. (1999), Origin and recycling processes of precipitating water over the eurasian continent: Experiments using an atmospheric general circulation model, *J. Geophys. Res.*, *104*(D2), 1957–1972.

Peixoto, J., and A. Oort (1992), *Physics of Climate*, Am. Inst. of Phys., N. Y.

Qian, Y., et al. (2015), Parametric sensitivity analysis of precipitation at global and local scales in the community atmosphere model CAM5, *J. Adv. Model. Earth Syst.*, *7*(2), 382–411.

Sodemann, H., and A. Stohl (2009), Asymmetries in the moisture origin of Antarctic precipitation, *Geophys. Res. Lett.*, *36*, L22803, doi:10.1029/2009GL040242.

Sodemann, H., and A. Stohl (2013), Moisture origin and meridional transport in atmospheric rivers and their association with multiple cyclones, *Mon. Weather Rev.*, *41*, 2850–2868.

Sodemann, H., H. Wernli, and C. Schwierz (2009), Sources of water vapour contributing to the elbe flood in august 2002—A tagging study in a mesoscale model, *Q. J. R. Meteorol. Soc.*, *135*(638), 205–223.

Stohl, A., and P. James (2004), A Lagrangian analysis of the atmospheric branch of the global water cycle. Part I: Method description, validation, and demonstration for the August 2002 flooding in Central Europe, *J. Hydrometeorol.*, *5*, 656–678.

Stohl, A., and P. James (2009), A Lagrangian analysis of the atmospheric branch of the global water cycle. Part ii: Moisture transports between earth's ocean basins and river catchments, *J. Hydrometeorol.*, *6*(6), 961–984.

Trenberth, K. (1998), Atmospheric moisture residence times and cycling: Implications for rainfall rates and climate change, *Clim. Change*, *39*(4), 667–694.

Trenberth, K. (1999), Atmospheric moisture recycling: Role of advection and local evaporation, *J. Clim.*, *12*, 1368–1381.

Trenberth, K., J. Fasullo, and J. Mackaro (2011), Atmospheric moisture transports from ocean to land and global energy flows in reanalyses, *J. Clim.*, *24*, 4907–4925.

van der Ent, R., H. H. G. Savenije, B. Schaefli, and S. Steele-Dunne (2010), Origin and fate of atmospheric moisture over continents, *Water Resour. Res.*, *46*, W09525, doi:10.1029/2010WR009127.

Wehner, M., et al. (2014), The effect of horizontal resolution on simulation quality in the community atmospheric model, CAM5.1, *J. Adv. Model. Earth Syst.*, *6*, 980–997, doi:10.1002/2013MS000276.

Werner, M., M. Heimann, and G. Hoffmann (2001), Isotopic composition and origin of polar precipitation in present and glacial climate simulations, *Tellus, Ser. B*, *53*(1), 53–71.

Yang, B., et al. (2013), Uncertainty quantification and parameter tuning in the CAM5 Zhang-Mcfarlane convection scheme and impact of improved convection on the global circulation and climate, *J. Geophys. Res. Atmos.*, *118*, 395–415, doi:10.1029/2012JD018213.